Na$_{2/7}$Gd$_{4/7}$MoO$_4$: a Modulated Scheelite-Type Structure and Conductivity Properties

V. Morozov,*,[†] A. Arakcheeva,[‡,§] B. Redkin,[⊥] V. Sinitsyn,[⊥] S. Khasanov,[⊥] E. Kudrenko,[⊥] M. Raskina,[†] O. Lebedev,[¶] and G. Van Tendeloo[∥]

[†]Chemistry Department, Moscow State University, 119991 Moscow, Russia

[‡]Laboratoire de Crystallographie, École Polytechnique Fédérale de Lausanne, BSP, CH-1015 Lausanne, Switzerland

[§]Phase Solutions Ltd., CH-1012 Lausanne, Switzerland

[⊥]Institute of Solid State Physics, 142452 Chernogolovka, Russia

[¶]Laboratoire CRISMAT, UMR 6508 CNRS ENSICAEN, 6bd Maréchal Juin, 14050 Caen, France

[∥]EMAT, University of Antwerp, Groenenborgerlaan 171, B-2020 Antwerp, Belgium

Ⓢ *Supporting Information*

ABSTRACT: Scheelite-type compounds with the general formula $(A1,A2)_n[(B1,B2)O_4]_m$ ($^2/_3 \leq n/m \leq ^3/_2$) are the subject of large interest owing to their stability, relatively simple preparation, and optical properties. The creation of cation vacancies (□) in the scheelite-type framework and the ordering of A cations and vacancies can be a new factor in controlling the scheelite-type structure and properties. For a long time, cation-deficient Nd^{3+}:M$_{2/7}$Gd$_{4/7}$□$_{1/7}$MoO$_4$ (M = Li, Na) compounds were considered as potential lasers with diode pumping. They have a defect scheelite-type 3D structure (space group $I4_1/a$) with a random distribution of Li$^+$(Na$^+$), Gd^{3+}, and vacancies in the crystal. A Na$_{2/7}$Gd$_{4/7}$MoO$_4$ single crystal with scheelite-type structure has been grown by the Czochralski method. Transmission electron microscopy revealed that Na$_{2/7}$Gd$_{4/7}$MoO$_4$ has a (3 + 2)D incommensurately modulated structure. The (3 + 2)D incommensurately modulated scheelite-type cation-deficient structure of Na$_{2/7}$Gd$_{4/7}$MoO$_4$ [super space group $I\bar{4}$ ($\alpha-\beta 0,\beta\alpha 0)00$] has been solved from single-crystal diffraction data. The solution of the (3 + 2)D incommensurately modulated structure revealed the partially disordered distribution of vacancies and Na and Gd cations. High-temperature conductivity measurements performed along the [100] and [001] orientation of the single crystal revealed that the conductivity of Na$_{2/7}$Gd$_{4/7}$MoO$_4$ at T = 973 K equals $\sigma = 1.13 \times 10^{-5}$ Ω^{-1} cm^{-1}.
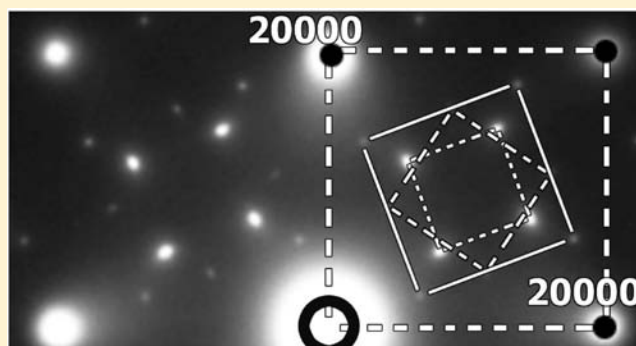
1. INTRODUCTION

White-light-emitting diodes (WLEDs), as the promising solid-state lighting source, have attracted much attention because of their high reliability, long lifetime, low energy consumption, and environmentally friendly characteristics.[1] The availability of WLEDs is expected to open up a great number of exciting new application fields such as white light sources to replace traditional incandescent and fluorescent lamps, backlights for portable electronics, medical and architecture lighting, and others.[2] Phosphor-converted WLEDs can be fabricated by employing blue/green/red tricolor phosphors excited by a near-ultraviolet (UV) (360−410 nm) InGaN-based LED, which can compete for applications requiring a high quality of light. The current tricolor phosphors for near-UV InGaN-LED chips are Y$_2$O$_2$S:Eu^{3+} for red, ZnS:(Cu$^+$ and Al^{3+}) for green, and BaMgAl$_{10}$O$_{17}$:Eu^{2+} for blue.[3] Unfortunately, the Y$_2$O$_2$S:Eu^{3+} red phosphor does not absorb efficiently in the near-UV region, and its brightness is about 8 times less than that of the green and blue phosphors. As a result, it is necessary to use a

phosphor mixture containing 80% red, 10% green, and 10% blue in order to obtain good color rendering. In addition, the lifetime of Y$_2$O$_2$S:Eu^{3+} is inadequate under near-UV irradiation because of its instability. Other known sulfide-based materials such as CaS:Eu^{2+}, SrY$_2$S$_4$:Eu^{2+}, and ZnCdS:Cu have similar disadvantages, such as chemical instability, likelihood to deliquesce, and strong corrosive H$_2$S gas production. Recently, considerable efforts have been devoted to the research on new materials used for WLEDs.

A large number of luminescent materials based on rare-earth ions or rare-earth host lattices have been invented as an alternative to the sulfide-based phosphors. Furthermore, interest in solid-state materials of vanadates,[4] phosphates,[5] molybdates, and tungstenates doped with rare-earth ions has significantly grown because of their long-wavelength properties and excellent chemical stability. During the past few years,

interest arose concerning rare-earth-doped molybdates and tungstates with a scheelite-type $(CaWO_4)$ structure because of their potential as WLED[6−10] and laser materials.[11−14] Molybdate and tungstate phosphors have broad and intense absorption bands due to charge transfer (CT) from oxygen to metal in the near-UV region. Therefore, it is necessary to develop highly efficient molybdate phosphors for WLED and laser applications.

Some scheelite-type compounds, such as $PbMoO_4$, $KGd(WO_4)_2$, $NaBi(WO_4)_2$, and MWO_4 (M = Pb, Cd, Ca), are well-known and are used, while other $MR(BO_4)_2$ [M = Li, Na, K, Ag; R = lanthanides (Ln), Y, Bi; B = W, Mo] single crystals are often proposed as potential red phosphors for WLED. For example, the emission peak intensities of $NaEu(WO_4)_2$[15] and $KGd_{0.75}Eu_{0.25}(MoO_4)_2$[16] are respectively about 8.5 and 3.5 times higher than that of $Y_2O_2S:Eu^{3+}$. $NaMY(MoO_4)_3:Eu^{3+}$ (M = Sr, Ca) phosphors have higher emission intensities (4.12−4.62 times) than that from the commercial red phosphor $CaS:Eu^{2+}$.[9]

Besides WLED and laser applications, cation-deficient scheelite-type compounds can be considered as good ion conductors.[17,18] For example, adding 5% and 15% Pr^{3+} to $PbWO_4$, inducing the formation of a cation-deficient scheelite-type compound, leads to an increased conductivity at 1073 K from 5.0×10^{-5} S cm^{-1} (for pure $PbWO_4$) to 1.40×10^{-2} and 2.40×10^{-2} S cm^{-1}, respectively. A 1.6 atom % Nd^{3+} doping of $PbWO_4$ makes the conductivity at 1073 K increase more than 2 orders, up to 7.16×10^{-3} S cm^{-1}. The ionic transport in such compounds results from migration of the point defects (vacancies or interstitials) on the cation or anion sublattice.

The $CaWO_4$ scheelite has tetragonal symmetry (space group $I4_1/a$).[19] This scheelite-type structure is adopted by a large family of compounds with composition ABO_4. Many different A and B cations with various oxidation states can easily be accommodated in the scheelite-type structure. Some examples, which demonstrate the ability of the scheelite-type structure to host cations with variable oxidation states, are $KReO_4$ and $AgIO_4$ (A$^+$ and B^{+7}), $CdMoO_4$ and $CaMoO_4$ (A^{+2} and B^{+6}), $BiVO_4$ and $YNbO_4$ (A^{+3} and B^{+5}), and $ZrGeO_4$ (A^{+4} and B^{+4}). Substitution of Ca^{2+} into $CaBO_4$ (B = W, Mo) by a combination of M$^+$ (M$^+$ = Li, Na) and R^{3+} (R = Ln, Y, Bi) leads to the formation of the double tungstates and molybdates $M_{0.5}R_{0.5}BO_4$[5,6,11−14,20−26] with a random distribution of M$^+$ and R^{3+} cations. It should be noted that the overwhelming majority of the studied scheelite-type compounds belong to the stoichiometric $(A1,A2)_n[(B1,B2)O_4]_n$ composition, i.e., cation:anion ratio = $(A1 + A2):(B1O_4 + B2O_4)$ = 1:1, leaving no possibility for vacancies in either the anionic (BO_4) or cationic (A) structural subsets.

However, scheelite-type compounds with a wide range of vacancies on the cationic site, with compositions characterized by different and not necessarily integer $(A1 + A2):(B1O_4 + B2O_4)$ ratios, can be prepared. An investigation of the phase formation in the system $M_2MoO_4–Ln_{2/3}MoO_4$ (M = Li, Na) revealed new phases $M_{1/8}Ln_{5/8}\square_{1/4}MoO_4$ [(M + Ln):MoO_4 ratio = 3:4] with a distorted scheelite-type structure in the region between $M_{0.5}Ln_{0.5}MoO_4$ and $Ln_{2/3}MoO_4$.[27,28] The creation of a cation vacancy ($\square$) in the scheelite-type framework and the ordering of A cations and vacancies can be a new parameter for monitoring the properties of scheelite-type compounds. The $Li_{2/7}Gd_{4/7}\square_{1/7}MoO_4$ crystal was reported in 1974 as a ferroelectric and paramagnetic material.[29] Subsequent publications supposed that $Li_{0.286}Gd_{0.571}MoO_4$[30]

and $Li_{0.3125}La_{0.5625}MoO_4$[31] had a defect scheelite-type structure (space group $I4_1/a$) with a random distribution of Li$^+$, Gd^{3+} (or La^{3+}), and vacancies in the crystal. An investigation of $Nd^{3+}:M_{2/7}Gd_{4/7}MoO_4$ (M = Li,[32] Na[33]) crystals showed that these cation-deficient scheelite-type compounds may be considered for a potential laser with diode pumping. The Eu^{3+}-doped $M_{2/7}Gd_{4/7}MoO_4$ (M = Li, Na)[34] phosphors are promising red-emitting phosphors pumped by near-UV and blue light. The intensity of the emission from $^5D_0$ to $^7F_2$ of $Na_{2/7}(Gd_{0.3}Eu_{0.7})_{4/7}MoO_4$ is about 5 times higher than that of $Y_2O_3:Eu^{3+}$.

Earlier transmission electron microscopy (TEM) allowed us to reveal that the real structure of $Ag_{1/8}Pr_{5/8}MoO_4$ was incommensurately modulated[35] and to believe that it was the first representative in a large family of incommensurately modulated scheelite-type compounds with the general formula $M_{x/8}Ln_{(16-x)/24}\square_{(4-x)/12}MoO_4$ (M = alkali metal, Ag; Ln = Ln, Y, Bi). The correlation between the number of cation vacancies and the ordering of A cations and vacancies in the scheelite-type framework with luminescent properties is shown for the system $Na_2MoO_4–Eu_2(MoO_4)_3$.[36] In this work, we determined for the first time, the cation-deficient (3 + 2)D incommensurately modulated scheelite-type structure of $Na_{2/7}Gd_{4/7}MoO_4$ from single-crystal diffraction data. Different physical properties of the $Na_{2/7}Gd_{4/7}MoO_4$ single crystal have also been investigated.

2. EXPERIMENTAL SECTION

2.1. Materials and Crystal Growth. The polycrystalline materials used for single-crystal growth were prepared by a solid-state reaction. A stoichiometric mixture of raw materials [Na_2CO_3, Gd_2O_3 (spectroscopic pure ≥99.995%), and MoO_3] was placed in a platinum crucible and annealed at 773−823 K for 15 h to decompose the carbonate. Then the annealed mixture was ground, mixed again, and heated at 1073 K for 15 h in air. Note that a $Na_{2/7}Gd_{4/7}MoO_4$ crystal doped with Nd^{3+} melts congruently at 1467 K.[33] The synthesized polycrystalline materials of $Na_{2/7}Gd_{4/7}MoO_4$ (NG$_2$M) were melted in a 40 × 40 mm^2 diameter platinum crucible using a 17 kHz frequency induction furnace. A small nonoriented $Na_{2/7}Gd_{4/7}MoO_4$ single-crystal bar was used as a seed. The growing temperature was accurately determined by repeated seeding trials. A $Na_{2/7}Gd_{4/7}MoO_4$ (NG$_2$M) single crystal up to 15 mm diameter and 20 mm length was grown at 1523 K by the Czochralski method at a pulling rate of 1−3 mm h^{-1} and a rotating rate of 20−50 rpm in a slightly oxidizing atmosphere. After growth, the crystal was drawn above the surface of the melt and cooled down to room temperature (T_R) at a rate of −20 K h^{-1}. The as-grown crystal was black in color because of an oxygen-deficient atmosphere[21] and needed to be annealed in air to reduce the color centers. A light-violet and transparent crystal was obtained after oxidative annealing at 1073 K for 12 h.

Two crystal slices, having a surface of 10 × 10 mm^2 and a thickness of approximately 2 mm, were cut perpendicular ([001] orientation) or parallel ([100] orientation) to the c axis, i.e., optical axis directions, and then optically polished to a thickness of 518 μm to to obtain parallel faces. The crystallographic orientation of the samples was determined using X-ray Laue back-reflection. Impedance spectroscopy measurements were performed on both polished crystal plates.

2.2. Characterization. The element content of the single crystal was determined by a wavelength-dispersive X-ray fluorescence (WDXRF) technique using a Thermo (Thermo Fisher Scientific Inc., Allschwil, Switzerland) ARL Optim'X fluorescence spectrometer [air-cooled X-ray tube with a rhodium anode and thin beryllium window (0.075 mm)] equipped with a SmartGonio goniometer (flow proportional and scintillation counters). The crystal plates were placed on a spectroscopically pure polypropylene film (6 μm thickness). WDXRF measurement was obtained under vacuum (2.5 Pa) over the wavelength range from F Kα to Ba Kα. WDXRF data for the standard

samples were used to set up the calibration curves. The *OptiQuant* software package was used for elemental content calculation, taking into account polypropylene film absorption.

Energy-dispersive X-ray (EDX) analysis and electron diffraction (ED) were obtained using a Philips CM20 microscope (Philips, Eindhoven, The Netherlands) with an Oxford INCA attachment (Oxford Instruments plc, Oxford, U.K.). TEM samples were prepared by mechanically grinding the crystal plate to a thickness of about 15 μm, followed by ion-beam milling. Ion milling was done by 4 keV Ar^+ bombardment with the guns oriented under grazing incidence with respect to the surface. The EDX analysis results were based on the Gd_L and Mo_L lines in the spectra. The Gd:Mo ratio was confirmed by local EDX analysis in the transmission electron microscope, in combination with ED patterns for structure identification of the crystal plates with [001] and [100] orientation.

ED and high-resolution TEM (HRTEM) were carried out with a JEOL 4000EX microscope (JEOL, Tokyo, Japan) operated at 400 kV. Measurements were performed along the [001] and [100] zone axes. Computer simulations of the HRTEM images were performed using the *CrystalKit* and *MacTempas* software (Total Resolution LLC, Berkeley, CA) packages.

The single-crystal X-ray data were collected at room temperature on a Oxford Diffraction Gemeni R diffractometer with Mo Kα radiation ($\lambda = 0.7107$ Å) with a CCD detector using the $\omega-\theta$ scanning mode. A total of 234208 reflections within the range of $2.45 \leq \theta \leq 40.29°$, at $-10 \leq h \leq 10$, $-10 \leq k \leq 10$, $-20 \leq l \leq 20$, $-1 \leq m \leq 1$, and $-1 \leq n \leq 1$, were measured. The absorption correction was carried out empirically using the *SCALE3 ABSPACK* program from the diffractometer software. NG_2M structure determination and refinement were carried out using the *JANA2006*[37] program package. Illustrations were produced with the *JANA2006* program package in combination with the program *DIAMOND*.[37]

Calorimetric studies have been carried out in the temperature range from 378 to 900 K using a PerkinElmer DSC-7 microcalorimeter (PerkinElmer, Waltham, MA). A single crystal (weight ~20 mg) was heated at a rate of 20 K min^{-1} in an argon atmosphere. The heat capacity was calculated using the *POLARIS* software. Dilatometric studies were carried out using a PerkinElmer TMA-7 thermoanalyzer with an argon atmosphere in the regime of heating with the same rate (20 K min^{-1}) as in the case of the calorimetric studies. Samples with a thickness of 0.531 mm were cut from single crystals parallel to the *c* plane and measured at temperatures from 574 to 1067 K.

A platinum paste was put on the flat surfaces of the crystal plates. Additional sintering at 973 K for 60 min was accomplished to ensure good electrical contact between the sample and metal electrodes. Electrical characterization was performed in a Probostat measurement cell[38] with a two-point electrode setup. A β impedance analyzer[39] was used for all impedance measurements in the frequency range from 75.6 mHz to 3 MHz with an applied oscillation voltage of 0.5 V (root mean square). High-temperature conductivity measurements at 373−973 K were performed while the cell was located in a tubular Novocontrol HT resistance furnace (Novocontrol Technologies, Hundsangen, Germany). The temperature was controlled by a Pt/Pt−10% Rh thermocouple inside the cell, placed close to the sample. Measurement processes were controlled electronically by the *WinDETA* package of programs.

3. RESULTS AND DISCUSSION

3.1. Elemental Composition. Elemental analysis performed by WDXRF for the plate with [001] orientation gave the following for the Na, Gd, and Mo contents (recalculated to the corresponding oxides): 3.54 ± 0.35 wt % Na_2O, 40.65 ± 0.25 wt % Gd_2O_3, and 55.81 ± 0.35 wt % MoO_3. The oxide ratio was found to be $Na_2O:Gd_2O_3:MoO_3 = 1.03:2.02:7$. This is close to the $Na_{2/7}Gd_{4/7}MoO_4$ composition (Na:Gd:Mo = 2.06:4.04:7).

The elemental composition was confirmed by EDX analysis using a transmission electron microscope together with ED

patterns for each crystallite. EDX analysis was performed at four points for 10 different crystallites. The cation ratio was found to be Gd:Mo = 4.2(2):7 (37.8 ± 1.6 atom % Gd and 62.3 ± 0.9 atom % Mo). This is again close to the bulk $Na_{2/7}Gd_{4/7}MoO_4$ composition determined by WDXRF and reveals a homogeneous elemental distribution in the sample.

3.2. ED Study. The $[1\bar{1}0]^*$ and $[100]^*$ ED patterns for NG_2M are similar to the published ED patterns for $Ag_{1/8}Pr_{5/8}MoO_4$,[35] $KNd(MoO_4)_2$,[40] and $KSm(MoO_4)_2$,[41] while the $[001]^*$ ED pattern for NG_2M shows a considerable difference (Figure 1). All strong reflections in the ED patterns
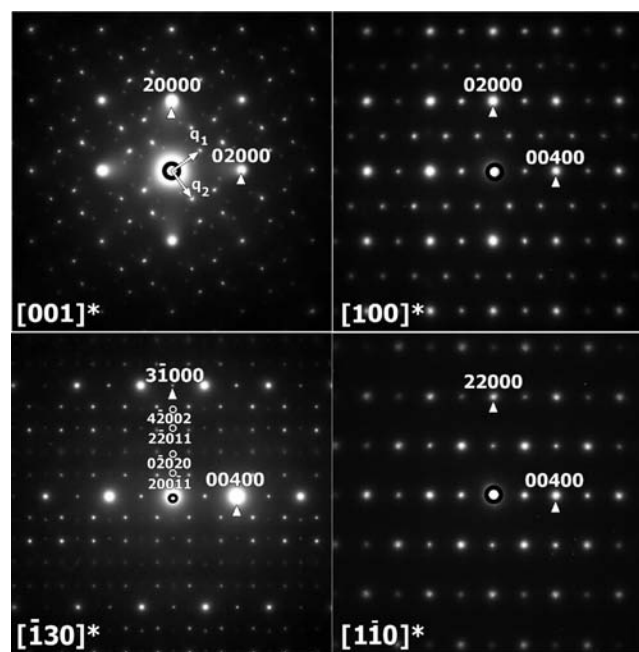
**Figure 1.** $[001]^*$, $[\bar{1}30]^*$, $[100]^*$ and $[1\bar{1}0]^*$ ED patterns of the incommensurately modulated $Na_{2/7}Gd_{4/7}MoO_4$ phase.

for NG_2M correspond to the scheelite-type tetragonal subcell with unit cell parameters $a_t \approx 5.22$ Å and $c_t \approx 11.45$ Å. The $[100]^*$, $[1\bar{1}0]^*$, and $[\bar{1}30]^*$ ED patterns exhibit even $00l$: $l \neq 4n$ reflections forbidden by the $I4_1/a$ symmetry usually observed for scheelite-type compounds. The intensities of even $00l$: $l \neq 4n$ reflections are systematically lower than $00l$: $l = 4n$ (Figure 1); however, tilting of the sample around the $[00l]$ direction did not lead to a vanishing of these reflections. Therefore, these spots could not be attributed to double diffraction. The observation of $00l$: $l \neq 4n$ reflections on the ED patterns testifies that the symmetry of NG_2M should be changed from $I4_1/a$ to $I\bar{4}$. This changing of symmetry from $I4_1/a$ to $I\bar{4}$ has been observed earlier for other scheelite-type compounds: $LiYb(MoO_4)_2$,[24] $NaGd(WO_4)_2$,[25] and $NaBi(WO_4)_2$.[26]

In contrast to the $[001]^*$ ED pattern for incommensurately modulated $Ag_{1/8}Pr_{5/8}MoO_4$ and $KNd(MoO_4)_2$,[35,40] the weaker reflections observed in the $[001]^*$ ED pattern for NG_2M cannot be indexed with four $hklm$ integers, as given by the diffraction wave vector $\mathbf{H} = h\mathbf{a}^* + k\mathbf{b}^* + l\mathbf{c}^* + m\mathbf{q}$, where $\mathbf{q}$ is a modulation vector. The indexation schemes of the $[001]^*$ ED pattern of scheelite-type structures are shown in Figure 2. The presence of $hkl11$ reflections in the $[001]^*$ ED pattern proves that the NG_2M structure is tetragonal with two modulation vectors because these weaker reflections cannot be indexed in
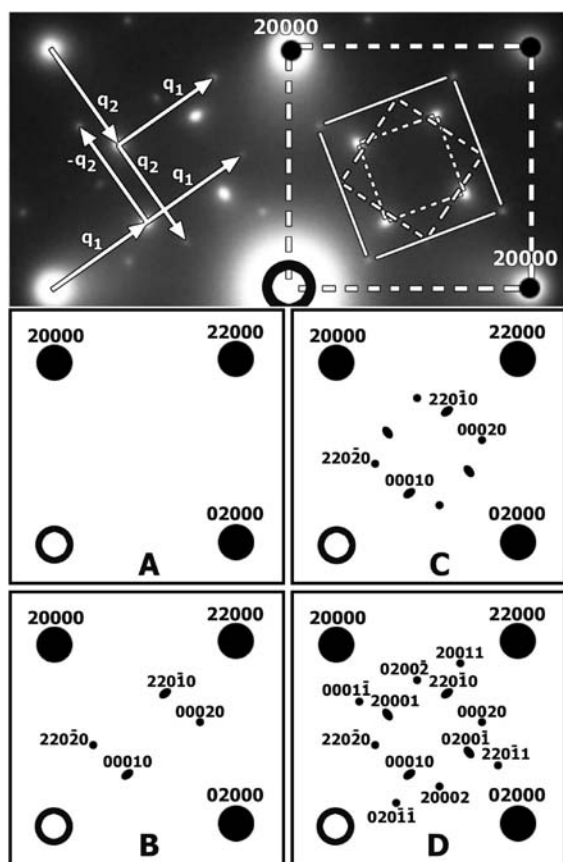
Figure 2. Part of the $[001]^*$ ED pattern of $Na_{2/7}Gd_{4/7}MoO_4$ and indexation schemes of the $[001]^*$ ED pattern of scheelite-type structures: (A) $CaWO_4$ structure with 3D space group $I4_1/a$; (B) incommensurately modulated structure with $(3 + 1)$D monoclinic SSG $I2/b(\alpha\beta0)00$; (C) incommensurately modulated structure (pseudotetragonal) with the $(3 + 1)$D monoclinic SSG $I2/b(\alpha\beta0)00$ + 90° twinning; (D) incommensurately modulated structure with the $(3 + 2)$D tetragonal SSG.

the monoclinic $(3 + 1)$D structure. The indexing of the ED patterns for NG_2M could only be made with five $hklmn$ indexes given by the diffraction wave vector $\mathbf{H} = h\mathbf{a}^* + k\mathbf{b}^* + l\mathbf{c}^* + m\mathbf{q}_1 + n\mathbf{q}_2$, with modulation vectors $\mathbf{q}_1 \approx 0.54\mathbf{a}^* + 0.81\mathbf{b}^*$ and $\mathbf{q}_2 \approx -0.81\mathbf{a}^* + 0.54\mathbf{b}^*$. The reflections with $m, n = 0$ and $m, n \neq 0$ correspond to the main and satellite reflections, respectively (Figure 2D). Because the $\mathbf{q}_1$ and $\mathbf{q}_2$ vector components are significantly different from any rational value, the structure can be considered as incommensurately modulated. Thus, ED patterns of NG_2M can be completely indexed with unit cell parameters $a \approx 5.22$ Å and $c \approx 11.45$ Å and two modulation vectors $\mathbf{q}_1 \approx 0.54\mathbf{a}^* + 0.81\mathbf{b}^*$ and $\mathbf{q}_2 \approx -0.81\mathbf{a}^* + 0.54\mathbf{b}^*$. It should be noted that the first-order satellite reflections ($hk010$ and $hk001$) are slightly elongated along the respective modulation vectors $\mathbf{q}_1$ and $\mathbf{q}_2$. The slight deformation of the $hk010$ and $hk001$ spots can be associated with a small local variation in the modulation vector values.

3.3. Crystal Structure Determination. In accordance with the ED study, NG_2M exhibits an incommensurately modulated structure. The basic concepts of the superspace theory for structural analysis of incommensurately modulated crystals and incommensurate composite crystals were first suggested by De Wolf et al.[42] and were followed up by Jansen et al. and Van Smaalen.[43]

A light-violet crystal ($0.1 \times 0.15 \times 0.2$ mm^3) of NG_2M was used for single-crystal X-ray data collection. The crystal for data collection was preliminarily rolled to a spherical form. The experimental details are summarized in Table 1. NG_2M

Table 1. Crystallographic Data for $Na_{2/7}Gd_{4/7}MoO_4$

Crystal Data	
chemical formula	$Na_{2/7}Gd_{4/7}MoO_4$
fw	256.4
temperature (K)	293
cryst syst	tetragonal
$(3 + 2)$D group of symmetry	$I\bar{4}(\alpha-\beta0,\beta\alpha0)00$
Lattice Parameters	
a (Å)	5.2127(2)
c (Å)	11.4523(11)
V (Å^3)	311.18(3)
$\mathbf{q}_1$ vector	$0.5644\mathbf{a}^* + 0.7976\mathbf{b}^*$
$\mathbf{q}_2$ vector	$-0.7976\mathbf{a}^* + 0.5644\mathbf{b}^*$
Z	4
calcd density, D_x (g cm^{-3})	5.4705
color	light-violet
cryst size (mm^3)	$0.1 \times 0.15 \times 0.2$
Data Collection	
diffractometer	Oxford Diffraction Gemini R
radiation type/wavelength (λ, Å)	Mo Kα/0.7107
radiation monochromator	graphite
θ range (deg)	2.45−40.29
$hklmn$ ranges	$-10 < h < 10$; $-10 < k < 10$; $-20 < l < 20$; $-1 < m < 1$; $-1 < n < 1$
total no. of reflns	234208
coverage (%)	99
no. of obsd reflns	91583
criteria of observation	$I > 3\sigma(I)$
no. of averaged reflns (obsd/all)	5418/8829
among them:	
main	932/986
first-order satellite reflns	3401/3924
second-order satellite reflns	1085/3919
vectors of waves included in refinement (notations)	$\mathbf{q}_1$ (1, 0), $\mathbf{q}_2$ (0, 1), $-\mathbf{q}_1 + \mathbf{q}_2$ (−1, 1), $\mathbf{q}_1 + \mathbf{q}_2$ (1, 1)
no. of refined param	250
R and R_w, % (R_{obs}/R_{all})	3.49/5.38 and 4.73/4.89
among them:	
main	3.31/3.37 and 5.92/5.93
first-order satellite reflns	3.23/3.79 and 3.84/3.90
second-order satellite reflns	11.02/12.27 and 35.28/15.08
matrixes of twins	(100/010/001), (−100/0−10/00−1)
coefficients of twins	0.507(5), 0.493(5)
GOF (obsd/all)	2.46/2.02
max/min residual electron density (e Å^{-3})	3.61/−1.40

structure determination and refinement were carried out in the $(3 + 2)$D super space group (SSG) $I\bar{4}(\alpha-\beta0,\beta\alpha0)00$, which has been identified according to the systematic extinctions ($hklmn$: $h + k + l + m + n \neq 2p$) observed within 234208 reflections indexed with the refined tetragonal lattice parameters $a = 5.2127(2)$ Å, $c = 11.4523(11)$ Å, $\mathbf{q}_1 = 0.5644(1)\mathbf{a}^* + 0.7976(1)\mathbf{b}^*$, and $\mathbf{q}_2 = -0.7976(1)\mathbf{a}^* + 0.5644(1)\mathbf{b}^*$.
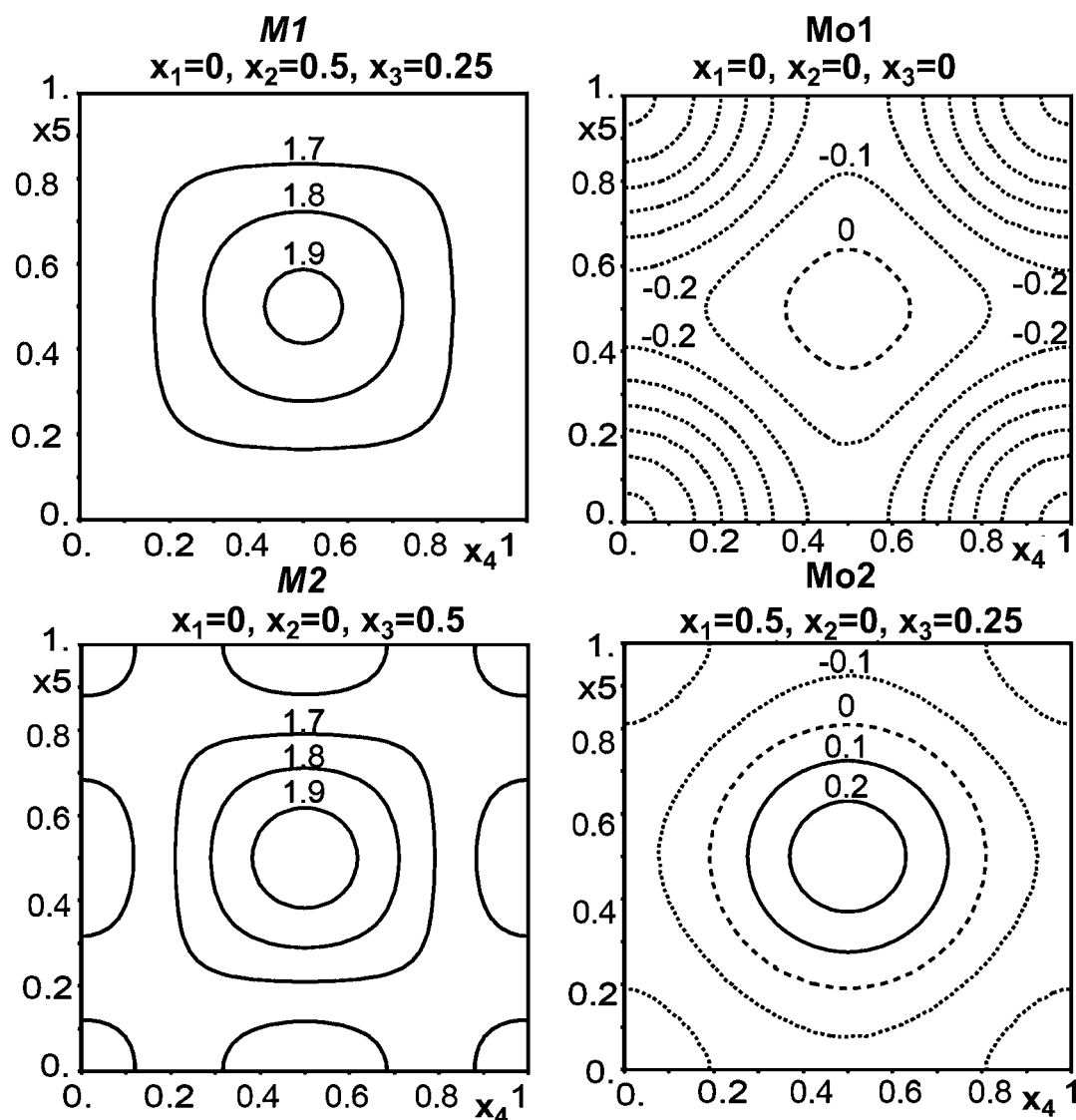
**Figure 3.** x_4x_5 section of the residual electron density (e Å^{-3}) in the vicinity of the M1, M2, Mo1, and Mo2 positions. Full, dashed, and dotted lines show positive, zero, and negative values of the electron density, respectively.

The initial atomic coordinates of an average model of the NG$_2$M structure have been deduced from the CaWO$_4$ structure (space group $I4_1/a$), assuming that the A position is statistically occupied by Na and Gd instead of Ca and the B position is occupied by Mo instead of W. After structural transformation from $I4_1/a$ to $I\overline{4}$, each atomic position appears as doubly split. Hence, the average NG$_2$M structure model contains two A positions, M1 and M2, statistically occupied by Na1, Gd1, Na2, and Gd2, respectively. The atomic occupation coefficients have been constrained according to the results of chemical analysis: (Na1 + Na2):(Gd1 + Gd2) = 1:2.

Refinement of the atomic coordinates and their modulation (Table S1 in the Supporting Information) has been executed along with a refinement of the occupation waves corresponding to Na1, Na2, Gd1, and Gd2. The refined Fourier amplitudes of the occupation modulation waves are listed in Table S2 in the Supporting Information. The ut plots of the occupation modulation functions of the M positions are shown in Figure 3 for Gd and Na separately. A rich experimental data collection [5456 reflections with $I > 3\sigma(I)$] allowed us to refine the anisotropic atomic displacement parameters and their modu-

lations (Table S3 in the Supporting Information). The number of reflections per one refined parameter remained more than 20 (Table 1). The reliability factor R_{all} = 3.59% shows a good agreement between the calculated and experimental intensities of all diffraction reflections including satellite reflections. Other numerical characteristics illustrating the quality of the structure refinement are presented in Table 1. A selection of the relevant interatomic distances and angles in the MoO$_4$ tetrahedra are presented in Table S4 in the Supporting Information. Tables S1−S4 and other details of the structure refinement are available in the Supporting Information.

The most interesting issue of the structure determination concerns distribution of the A cations on the M1 and M2 positions. The residual electron density is shown in Figure 3. This distribution is partially ordered. The M2 position appears as practically fully occupied by an approximately equivalent amount of Na and Gd, 0.4629(13)Na2 and 0.5124(4)Gd2 (Table S2 in the Supporting Information), in a complementary manner (Figure 4c,d). The local occupation of M2 is varied from pure Gd (0.98Gd + 0Na at t = 0.45 and u = 0.8 in Figure 4c,d) to pure Na (0.98Na + 0Gd at t = 0.95 and u = 0.3 in
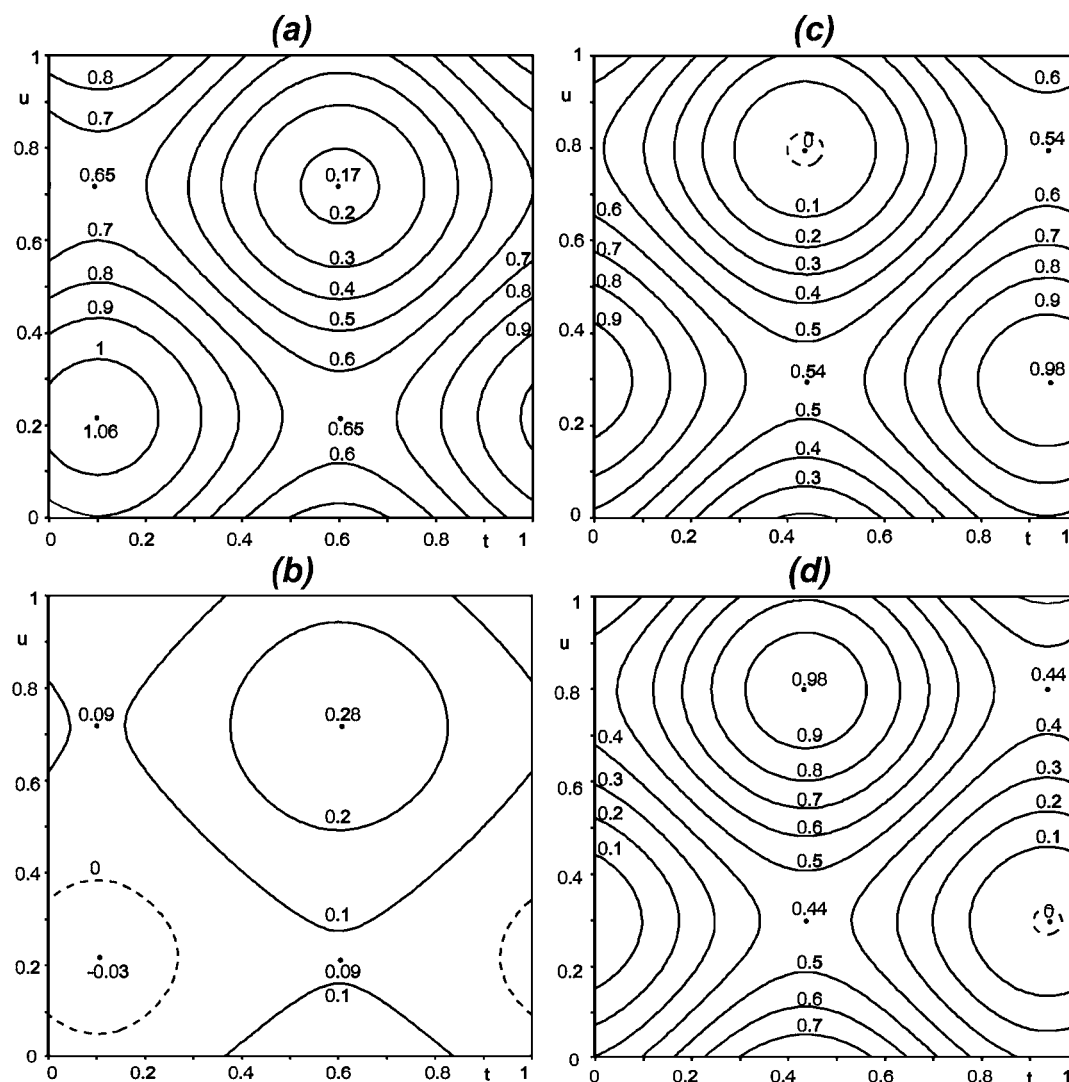
Figure 4. *ut* plot of the occupation modulation functions of Gd1 (a) and Na1 (b) on the M1 position and Gd2 (c) and Na2 (d) on the M2 position. Full, dashed, and dotted lines show positive, zero, and negative values of occupation, respectively. Minimum of the position occupation, 0.17Gd1 (a) + 0.28Na1 (b), and respectively, and maximum, 0.55, vacancies are observed on M1. No vacancies can be observed on M2 with complementary occupation modulation functions of Gd2 (c) and Na2 (d).

Figure 4c,d). Vacancies are observed only in the M1 position (Figure 4a,b) with variation from 0.26 (0.65Gd + 0.09Na at t = 0.6 and u = 0.22 in Figure 4a,b) to 0.55 (0.17Gd + 0.28Na at t = 0.6 and u = 0.72 in Figure 4a,b).

The residual electron density maps calculated in the vicinity of the A (M1 and M2 positions) and B (Mo1 and Mo2) cations are shown in Figure 3 as the $x_4 x_5$ sections. A relatively higher residual electron density (ρ_{max} = 1.9 e Å^{-3}) is observed in the vicinity of the M positions compared to the Mo positions (ρ_{max} = ±0.2 e Å^{-3}). Two types of functions for the (3 + 1)D incommensurately modulated structure can be used for the distribution function of atoms in the superspace: a Crenel function and a complementary wave. A relatively higher residual electron density is observed in the vicinity of the M positions and can be explained by the approximation of the M position occupation with the wave functions (Figure 4). Probably, some other occupation function (for example, a Crenel function), which allows the local presence of either a Na or Gd atom, could better fit the occupation of the M positions. However, such an opportunity is not available in *JANA2006* for the two-**q**-vector data set.[37]

The Supporting Information has been sent to the Fachinformationzentrum Karlsruhe, Abteilung PROKA, 76344 Eggenstein-Leopoldshaften, Germany, as No. 423588 and can be obtained by contacting the FIZ (quoting the article details and the corresponding SUP number).

3.4. Structure of Na$_{2/7}$Gd$_{4/7}$MoO$_4$. Using the *JANA2006* program package in combination with *DIAMOND*,[37] the following procedure has been applied for the (3 + 2)D incommensurate structure visualization: (i) starting with t_0 = 0, a portion of a 20 × 20 × 1 unit cell has been selected for drawing; (ii) the positional parameters of all atoms appearing in the selected part have been calculated; (iii) this part of the structure is presented as a unit cell with *P*1 symmetry in CIF format and used for the structure visualization. This portion of the structure is not periodic and is not supposed to be translated in the aperiodic directions along *a* and *b*. Hence, the cation ordering is illustrated only in a portion of the *ab* projection of the (3 + 2)D modulated Na$_{2/7}$Gd$_{4/7}$MoO$_4$ structure in Figure 5.

The scheelite-type ABO$_4$ structure is made up of AO$_8$ polyhedra and BO$_4$ tetrahedra sharing common vertices. The
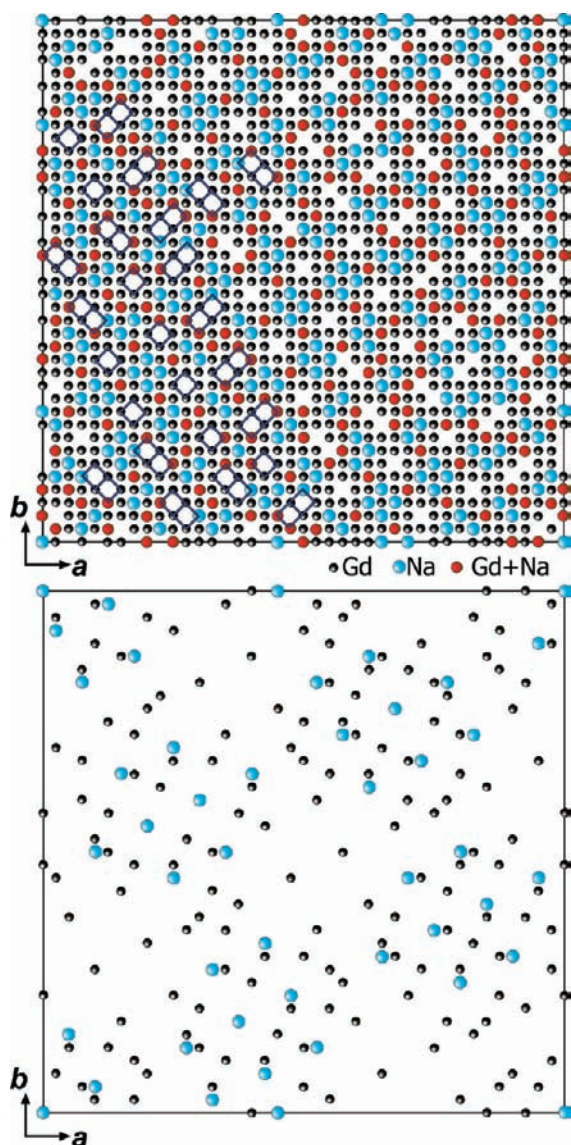
Figure 5. Cation ordering in the $(3 + 2)$D incommensurately modulated $Na_{2/7}Gd_{4/7}MoO_4$ structure. A portion of the *ab* projection is shown for Gd and Na, with the occupancy being more than 0.4 (top) and more than 0.9 (bottom) for each atom separately. MoO_4 tetrahedra are missing. Top: the different colors of the spheres define different occupancies of the cationic position: blue indicates the condition Na $\geq$ 0.4 and Gd < 0.4; gray indicates the condition Na < 0.4 and Gd $\geq$ 0.4; red indicates the condition Na $\geq$ 0.4 and Gd $\geq$ 0.4; absence of a sphere means the position occupation is less than 0.45. Bottom: only positions practically fully occupied ($\geq$0.9) by Na (blue) or Gd (gray) are shown. Blue squares select vacancies in the structure.

edge-sharing AO_8 polyhedra form a 3D framework. The main specific feature of the cation-deficient NG_2M structure is the partially disordered distribution of Na and Gd cations on the A site such as in $KSm(MoO_4)_2$,[41] in contrast to $KNd(MoO_4)_2$,[40] where K and Nd are completely ordered. The substitution of Ca^{2+} by Na^+ and Gd^{3+} cations in $CaMoO_4$ leads to the formation of cation vacancies in the A position so that $^1/_7$ of these positions are vacant in NG_2M. The ordering of the cation vacancies in NG_2M differs from the one in $Ag_{1/8}Pr_{5/8}MoO_4$,[35] where the structure can be considered as consisting of groups of five AO_8 (A = Pr, Ag) polyhedra alternating with two cation vacancies. This ordering (five AO_8 polyhedra + two vacancies)

is distorted by the formation of only one vacancy. In the NG_2M framework, the alternation of blocks with two vacancies is distorted by the formation of blocks with only one vacancy (Figure 5).

The MoO_4 tetrahedra appear as stable enough rigid units: Mo1–O distances vary from 1.749(6) to 1.792(6) Å with an average value of 1.772(6) Å; Mo2–O distances vary from 1.748(6) to 1.802(6) Å with an average value of 1.772(6) Å; the O–Mo–O angles vary from 104.9(3) to 119.6(3)° with average values 106.8–114.7°. Both M1 and M2 positions are surrounded by eight O atoms. Variation of the M–O distances is larger in the M2 polyhedra (from 2.373 to 2.565 Å) than in the M1 ones (from 2.379 to 2.563 Å). This fact correlates with the presence of vacancies at the M1 position.

3.5. HRTEM. HRTEM observations were performed at room temperature along the most informative [001] direction, where the structure of $Na_{2/7}Gd_{4/7}MoO_4$ can be also interpreted in terms of columns of A cations and MoO_4 groups. Figure 6 shows a [001] HRTEM image of the NG_2M crystal. The Fourier transform (FT) obtained from the HRTEM image exhibits a spot distribution similar to that of the ED pattern in Figure 1, indicating that the modulation features remain intact under the e-beam during the measurements. The crystal is well crystalline and free of stacking faults or any defects and exhibits a complex contrast due to the possible 3D domain structure.

In order to enhance the signal-to-noise ratio in the HRTEM image and clarify the nature of the ED spots, Fourier filtering was applied using a Bragg mask. The mask size was chosen in such a way that no structural information was lost but also such that no artifacts were introduced. The similarity of the filtered (Figure 6c) and experimental (Figure 6a) HRTEM images is proof of a correct filtering procedure. Figure 6b shows a filtered HRTEM image using only the basic 20000 and 02000 spots. Even after filtering, the observed image and the images calculated based on the X-ray data do not match, which points toward a more complicated structure induced by modulation. Figure 6c shows a filtered HRTEM image of NG_2M using basic as well as modulated reflections. However, the contrast is quite complicated and consists of square blocks of brighter dots (marked by a white square in the enlargement of Figure 6a). It is difficult to find any ordering of these blocks within the present crystal, which can be explained by the 3D domain structure resulting from overlapping domains on the projected image. A filtered image using only the modulated spots (Figure 6d) provides more evidence for the domain-type structure and confirms our assumption.

3.6. Physical Properties of $Na_{2/7}Gd_{4/7}MoO_4$. The temperature dependence of the specific heat, C_p, of a NG_2M single crystal is shown in Figure 7a. The C_p value increases monotonically from ~147 to ~181 J mol^{-1} K^{-1} in the temperature range 378–798 K. The measured C_p values of $Na_{2/7}Gd_{4/7}MoO_4$ are close to those of the rare-earth molybdates $R_{2/3}MoO_4$ (R = Pr, Nd, Sm, Eu, Gd, Tb, Dy).[44] The C_p dependence shows an anomalous behavior at temperatures from 802 to 858 K with a knee at T_{tr} = 843 ± 3 K. In view of the nonmonotonic dependence of C_p in a wide temperature interval around the transition point and the small magnitude of the anomaly at this point ($\Delta C_p/C_p \approx 3\%$), the calorimetric measurements did not allow us to reliably determine the heat effect and the type of phase transition.

Figure 7b shows the temperature dependence of the relative expansion, $\Delta L/L_0$, of the sample along the *c* axis. As seen from the figure, the $\Delta L/L_0$ value steeply decreases at a temperature
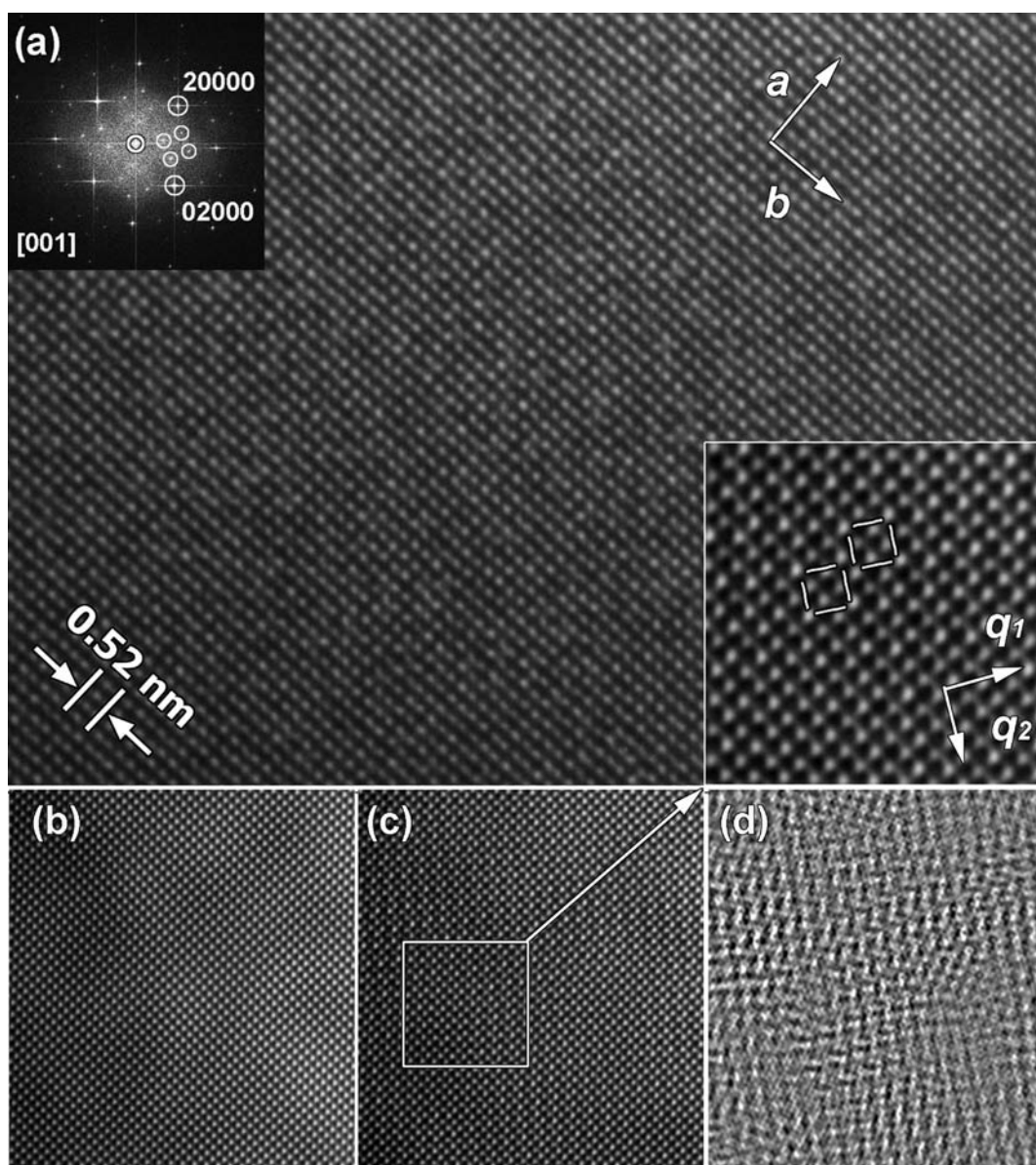
Figure 6. (a) [001] HRTEM image of $Na_{2/7}Gd_{4/7}MoO_4$ and corresponding FT. The lower inset shows a higher magnification (b) filtered HTREM image of part a; using a Bragg-mask filter, larger circles in the inset of part a were used to improve the signal-to-noise ratio. (c) Filtered image using Bragg reflections as well as satellite reflections (smaller circles in the inset of part a). (d) Filtered image using only satellite reflections.

of 847 ± 6 °C, coinciding (within experimental error) with the transition temperature T_{tr} determined by calorimetric measurements (Figure 7a). The jump in $\Delta L/L_0$ at the transition point only reaches ~0.12%. Results of the calorimetric and dilatometric measurements suggest that NG_2M should undergo a displacement-type phase transition of the first order close to the second order. It is worth noting that the coefficient of linear thermal expansion of the incommensurate phase constitutes ~2 $\times 10^{-5}$ K^{-1} in the temperature range 620−830 K (Figure 7b), which is typical of many complex oxides.[45]

The impedance spectra for the NG_2M single crystal with [001] orientation measured along the c axis at different temperatures are shown in Figure 8. At $T < 500$ K, the $Z'(\omega)-Z''(\omega)$ curve looks like a portion of a semicircle (Figure 8a) and completely corresponds to the bulk impedance of the crystal. The direct-current conductivity, σ, was calculated from the frequency dependencies of the complex impedance, $Z(\omega) = Z'(\omega) + iZ''(\omega)$. The high-frequency part of the complex

impedance is known to characterize the bulk transport properties of ionic conductors, whereas the charge migration through the boundary interfaces is a lower-frequency process.[46] An equivalent circuit can be presented as a bulk resistance R_b connected in parallel with a capacitor C if the system can be described with one relaxation time and as a bulk resistance R_b in parallel with a constant-phase element (CPE) $Q_b = Q_{b0}(j\omega)^{-n}$ if there is a distribution of relaxation times.[46] Analysis of the experimental data showed that the equivalent circuit (R_bQ_b; resistor in parallel with CPE in the Bouckamp notations[47]) provided a better fit within the whole studied temperature range. The n index in the CPE formulas changes from 0.86 to ~1, which is indicative of a weak dispersion in the time relaxation distribution. The bulk resistance, R_b, given by the intersection point of the impedance spectrum with the Z' real axis at $\omega \rightarrow 0$ is shown in Figure 8a. This allows us to calculate the specific conductivity as
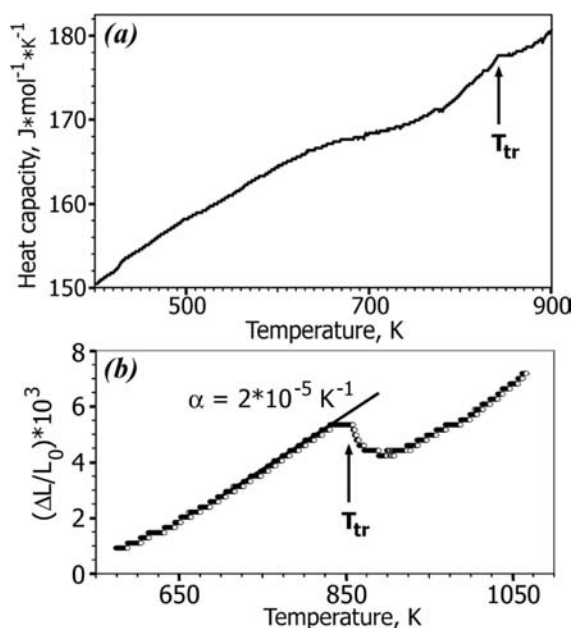
Figure 7. Heat capacity (a) and relative elongation $\Delta L/L_0$ ($L_0 = 0.531$ mm) of a $Na_{2/7}Gd_{4/7}MoO_4$ single crystal with $[001]$ orientation (b) as a function of the temperature. The arrow shows the temperature of a phase transition.

$$\sigma = \frac{1}{R_b} \frac{l}{S}$$

where l is the thickness and S the area of the sample.

The imaginary part of the impedance is maximal at a characteristic frequency ω_0 (Figure 8a), which can be determined from the equation

$$R_b Q_{b0} \omega_0^n = 1$$

The bulk resistance decreases with increasing temperature (σ increases) because ω_0 shifts to higher frequencies. This leads to two effects: an increase in the length of the arc of the $Z'(\omega)-Z''(\omega)$ semicircle characterizing the bulk part of the impedance and a decrease in the right cutoff with the Z' axis at $\omega \to 0$, which determines the bulk resistance R_b (Figure 8b). In addition to the high-frequency semicircle, a low-frequency semicircle appears on the $Z'(\omega)-Z''(\omega)$ dependencies, which describes the impedance of the electrode–electrolyte interface (Figure 8c). In this case, the equivalent circuit can be presented as two series-connected $R-Q$ circuits, $(R_bQ_b)(R_{in}Q_{in})$, where R_{in} and Q_{in} stand for the interface resistance and CPE. At high temperatures ($T > 920$ K), when the characteristic frequency ω_0 becomes comparable to or less than the maximum possible frequency of the measurements, the semicircuit arc of the bulk impedance starts to decrease from the high-frequency side (Figure 8d). The equivalent circuit remains the same, $(R_bQ_b)(R_{in}Q_{in})$, as in the previous case.

The conductivity σ calculated from the impedance spectra for the $[100]$ and $[001]$ orientations is shown in Figure 9 as an Arrhenius plot. As seen from the figure, there are several linear parts with different slopes in the dependencies of $\ln(\sigma T)$ versus $1000/T$. At high temperatures of $T > 800$ K (region I), the conductivity is nearly isotropic. The curve shows a knee at $T \approx 855$ K, which is close to the temperature T_{tr} of the anomalies in the specific heat and thermal expansion (Figure 7) and should therefore be attributed to the phase transition. The activation
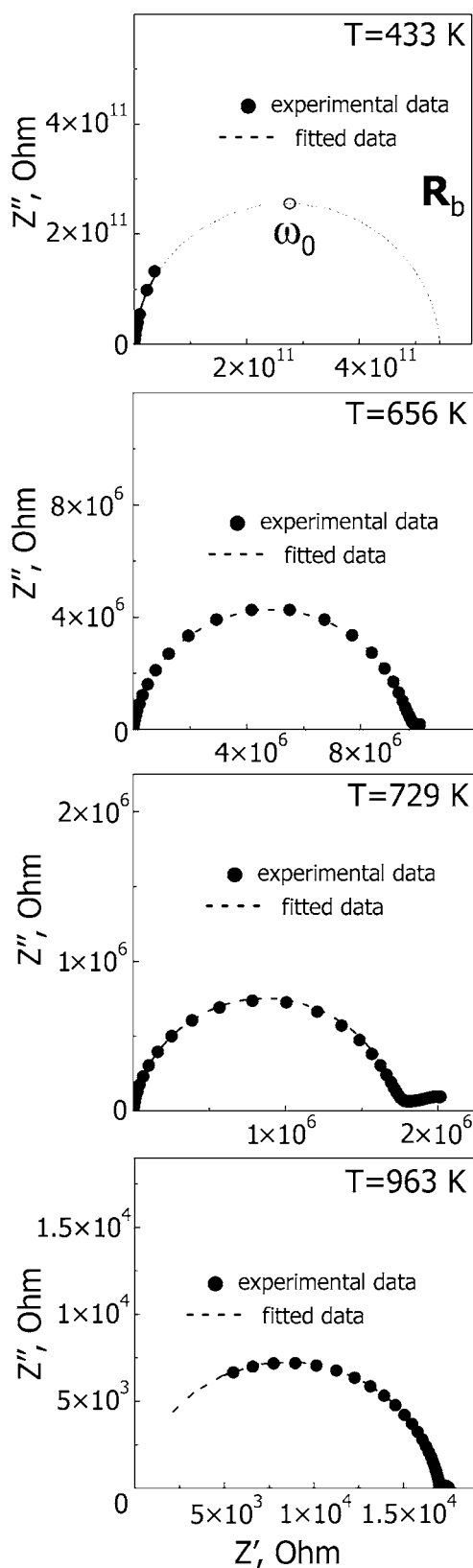
Figure 8. Impedance spectra of the $Na_{2/7}Gd_{4/7}MoO_4$ single crystal with $[001]$ orientation at different temperatures.

energy equals ~1.40 eV above the transition point and ~1.64 eV in the temperature range of 800–850 K. At temperatures below 800 K, the conductivity demonstrates a small anisotropy, $\sigma_{[001]}/\sigma_{[100]} \approx 1.5$–2.5 (depending on the temperature), and
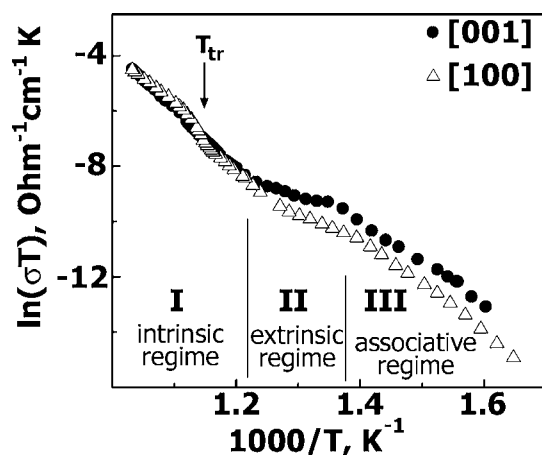
Figure 9. Temperature dependence of the conductivity for the [100] and [001] orientation of a $Na_{2/7}Gd_{4/7}MoO_4$ single crystal.

the dependences of both $\sigma_{[001]}$ and $\sigma_{[100]}$ components of the conductivity can be divided into two approximately linear portions with different slopes. The activation energies for these linear portions are ~0.76 eV for the intermediate region II and ~1.45 eV for the low-temperature region III.

Experimental data on the transport properties of $M_{2/7}Ln_{4/7}MoO_4$ (M = Li, Na, Ag; Ln = lanthanides) are missing in the literature. This is mainly due to the absence of single crystals of these compounds. The available experimental data on complex molybdenum and tungsten oxides with scheelite-type structure show that the conductivity of these crystals is mostly ionic and results from the migration of oxygen ions O^{2-}. It is therefore likely that the conductivity in the $Na_{2/7}Gd_{4/7}MoO_4$ crystals should also be due to the migration of defects on the oxygen sublattice. In this case, the conductivity is described by the Arrhenius-type expression

$$\sigma = \frac{A}{T} \exp\left(-\frac{E_a}{kT}\right)$$

where A and E_a are the preexponential factor and activation energy, respectively.

The total activation energy E_a is determined by the contributions from a number of thermally activated processes: migration, formation, association, and some others. The observed temperature dependencies of the ionic conductivity (Figure 9) can therefore be interpreted as follows. At high temperatures (region I), the conductivity is governed by thermally activated, intrinsic defects (most likely, by vacancies on the oxygen sublattice). In this temperature range, the total activation energy E_a is equal to the sum of the migration energy, E_m, and half of the formation energy of the moving defects, E_f; i.e., $E_a = E_m + \frac{1}{2}E_f$. The concentration of the intrinsic defects exponentially drops with decreasing temperature, and at a certain temperature, the contribution to the conductivity from the extrinsic defects begins to dominate. The extrinsic defects could be due to some uncontrolled impurities always presented in the crystal or due to the intentionally doped aliovalent ions. In this case, the total activation energy coincides with the migration energy ($E_a = E_m$). and the conductivity is called extrinsic conductivity. The transition from the intrinsic to the extrinsic regime is accompanied by a knee in the Arrhenius plot of the conductivity (Figure 9). The second knee on the $\ln(\sigma T)$ dependence is observed at a lower temperature. The behavior of the conductivity in this temperature range is usually

explained in terms of defects bound with impurities to form neutral pairs.[48] Such a temperature range of ionic transport is called the association regime, with the total activation energy $E_a = E_m + \frac{1}{2}E_b$, where E_b is the binding energy of the defect and aliovalent impurity.

By using the experimental data for the total activation energy in different temperature intervals, the above approach gives $E_m \approx 0.76$ eV, $E_f \approx 1.84$ eV, and $E_b \approx 1.38$ eV. Interestingly, the migration energy 0.76 eV proves to be close to the activation energy of the $Pb_{1-x}La_xMoO_4$ scheelite compound, in which a nonstoichiometry in the cation sublattice could also lead to extrinsic conductivity.[49] The conductivity of NG_2M at $T = 973$ K equals to $\sigma = 1.13 \times 10^{-5}$ Ω^{-1} cm^{-1}, which is significantly less than $\sigma = 10^{-3} - 10^{-2}$ Ω^{-1} cm^{-1} of the well-known oxygen conductors $Y{:}ZrO_2$ (YSZ) and $Ce{:}Gd_2O_3$ (GDC) at the same temperature.[50,51]

Early the high mobility of Na^+ in the complex molybdenum and tungsten oxides is shown for $Na_2MoO_4 - ZnMoO_4$,[52] Na_2MoO_4, and Na_2WO_4 crystals.[53] $Na_{2/7}Gd_{4/7}MoO_4$ studied in the present work is a cation-deficient compound with respect to the classical scheelite $CaWO_4$, in which $^1/_3$ of the divalent cation is substituted by a monovalent alkali-metal and $^2/_3$ by a trivalent rare-earth metal. Therefore, on the basis of the electroneutrality of the $Na_{2/7}Gd_{4/7}MoO_4$ compound, it can be considered as a scheelite-like phase with a chemical formula $Na_{2/7}Gd_{4/7}\square_{1/7}MoO_4$. Such a structure already contains crystallographic paths for the cation migration by alternating jumps of the Na^+ and Gd^{3+} ions. One can therefore expect the occurrence of a high cation conductivity along with the anion (oxygen) conductivity. However, a decisive conclusion about the mechanism of conductivity in $Na_{2/7}Gd_{4/7}MoO_4$ can only be made after very special, additional experiments, which is beyond the scope of the present paper.

4. SUMMARY

In scheelite-type research by X-ray diffraction, analysis of the reciprocal space between the main reflections (in single-crystal analysis) is often ignored, and one never considers the low-angle part of the powder X-ray diffraction (PXRD) patterns. Very often weak extra reflections observed in the whole PXRD patterns were completely ignored and not discussed.[18,54] The cation-deficient $Nd^{3+}{:}M_{2/7}Gd_{4/7}\square_{1/7}MoO_4$ (M = Li, Na) compounds, which are considered as potential lasers with diode pumping, were not an exception. They were thought to have a defect scheelite-type structure with space group $I4_1/a$ and with a random distribution of $Li^+(Na^+)$ and Gd^{3+} (Nd^{3+}) on the A position.[30−34] The present work interrupts this tradition by taking into account the information from the so-called satellite reflections located between the main reflections in the reciprocal space. Similar to the previously studied $K_{0.5}Nd_{0.5}MoO_4$ and $K_{0.5}Sm_{0.5}MoO_4$,[40,41] the present work shows that this information mainly concerns the ordering of cations and vacancies at the A position of the $Na_{2/7}Gd_{4/7}MoO_4$ scheelite-type structure. In other words, the main reason for structure modulations is the cation−vacancy ordering.

A $Na_{2/7}Gd_{4/7}MoO_4$ single crystal with scheelite-type structure has been grown by the Czochralski method. The $Na_{2/7}Gd_{4/7}MoO_4$ single crystal was studied by TEM and single-crystal X-ray diffraction, and the physical properties were measured. Using TEM has allowed us to gather new information about the real structure of the scheelite-type compounds. TEM revealed that the $Na_{2/7}Gd_{4/7}MoO_4$ structure is (3 + 2)D incommensurately modulated. It is the first time

that the (3 + 2)D incommensurately modulated scheelite-type structure is solved and the partial ordering of cations and vacancies revealed. Recently, the possibility of considering monoclinic and triclinic scheelite-type compounds as members of the (3 +1)D scheelite-type structure family with SSG $I2/b(\alpha\beta0)00$ has been postulated and discussed.[55] Both commensurately (3D) and incommensurately modulated scheelite-type compounds with a symmetry higher than monoclinic cannot be members of the scheelite (3 +1)D structure type, which is characterized by the monoclinic SSG $I2/b(\alpha\beta0)00$, even if the topology of their structure can be considered as pseudo-higher-symmetric.[55] It was also mentioned that the possibility of a supergroup has to be considered for the latter.[55] The tetragonal (3 + 2)D incommensurately modulated scheelite-type structure of $Na_{2/7}Gd_{4/7}MoO_4$ with SSG $I\bar{4}(\alpha-\beta0,\beta\alpha0)00$ gives an argument to consider scheelites as a (3 + 2)D structure type with SSG $I4_1/a(\alpha-\beta0,\beta\alpha0)00$. This (3 + 2)D structure type can uniquely describe the whole set of commensurately (3D) and incommensurately [(3 + 1)D and (3 + 2)D] modulated scheelite-type structures, however, without modulation along the c axis.

The transport properties of a new complex oxide, $Na_{2/7}Gd_{4/7}MoO_4$, have been investigated for the first time. A small anisotropy of the conductivity is observed in ranges II and III (Figure 9), where it is supposed to be of the extrinsic and associative type, correspondingly. The intrinsic conductivity (range I) is proved to be isotropic within experimental accuracy. According to the available experimental data, the ionic transport in complex molybdenum and tungsten oxides with scheelite-type structure is mainly due to the migration of oxygen point defects. Our experimental data allowed us to assume that the conductivity of the $Na_{2/7}Gd_{4/7}MoO_4$ crystal also results from the migration of defects in the oxygen sublattice. Nevertheless, it is worth noting that the conductivity of this crystal at temperatures near 700 °C is significantly lower than that of the well-known oxygen conductors YSZ and GDC.

ASSOCIATED CONTENT

S Supporting Information

X-ray crystallographic data in CIF format, table of final coordinates, isotropic displacement parameters, and Fourier amplitudes of the displacive modulation function for $Na_{2/7}Gd_{4/7}MoO_4$ (Table S1), table of positional occupancy and Fourier amplitudes of occupational waves for $Na_{2/7}Gd_{4/7}MoO_4$ (Table S2), table of anisotropic atomic displacement parameters and Fourier amplitudes of their modulations for the $Na_{2/7}Gd_{4/7}MoO_4$ structure (Table S3), and table of interatomic cation−oxygen distances (Å) and angles (deg) in the $[MoO_4]$ tetrahedra in $Na_{2/7}Gd_{4/7}MoO_4$ (Table S4). This material is available free of charge via the Internet at http://pubs.acs.org.

AUTHOR INFORMATION

Corresponding Author
*E-mail: morozov@tech.chem.msu.ru.

Notes
The authors declare no competing financial interest.

ACKNOWLEDGMENTS

REFERENCES

(1) Shur, M. S.; Zukauskas, A. *Proc. IEEE* **2005**, *93*, 1691.
(2) Yam, F. K.; Hassan, Z. *Microelectron. J.* **2005**, *36*, 129.
(3) Neeraj, S.; Kijima, N.; Cheetham, A. K. *Chem. Phys. Lett.* **2004**, *387*, 2.
(4) (a) Chen, X.; Zhuang, N. F.; Hu, X. L.; Zhuang, F. J.; Chen, J. Z. *Appl. Phys. B: Laser Opt.* **2007**, *88*, 449. (b) Wu, X.; Huang, Y.; Shi, L.; Seo, H. J. *Mater. Chem. Phys.* **2009**, *116*, 449.
(5) (a) Wang, J.; Zhang, Z.; Zhang, M.; Zhang, Q.; Su, Q.; Tang, J. *J. Alloys Compd.* **2009**, *488*, 582. (b) Huang, Y.; Ding, H.; Jang, K.; Cho, E.; Lee, H. S.; Jayasimhadri, M.; Yi, S.-S. *J. Phys. D: Appl. Phys.* **2008**, *41*, 095110. (c) Benhamou, R. A.; Bessiere, A.; Wallez, G.; Viana, B.; Elaatmani, M.; Daoud, M.; Zegzouti, A. *J. Solid State Chem.* **2009**, *182*, 2319. (d) Huang, Y.; Jiang, C.; Cao, Y.; Shi, L.; Seo, H. J. *Mater. Res. Bull.* **2009**, *44*, 793. (e) Liu, W.-R.; Chiu, Y.-C.; Yeh, Y.-T.; Jang, S.-M.; Chen, T.-M. *J. Electrochem. Soc.* **2009**, *156*, J165.
(6) Kim, T.; Kang, S. *J. Lumin.* **2007**, *122−123*, 964.
(7) Hwang, K.-S.; Jeon, Y.-S.; Hwangbo, S.; Kim, J.-T. *Opt. Appl.* **2009**, *39* (2), 375.
(8) Yan, B.; Wu, J.-H. *Mater. Chem. Phys.* **2009**, *116*, 67.
(9) Haque, M.; Lee, H.-I.; Kim, D.-K. *J. Alloys Compd.* **2009**, *481*, 792.
(10) Guo, C.; Gao, F.; Xu, Y.; Liang, L.; Shi, F. G.; Yan, B. *J. Phys. D: Appl. Phys.* **2009**, *42*, 095407.
(11) Lu, X.; You, Z.; Li, J.; Zhu, Z.; Jia, G.; Wu, B.; Tu, C. *Solid State Commun.* **2008**, *146*, 287.
(12) Li, X. Z.; Lin, Z. B.; Zhang, L. Z.; Wang, G. F. *Mater. Res. Innovations* **2006**, *10* (2), 50.
(13) Huang, X.; Wang, G. *J. Phys. D: Appl. Phys.* **2008**, *41*, 22540.
(14) Guo, W.; Chen, Y.; Lin, Y.; Gong, X.; Luo, Z.; Huang, Y. *J. Phys. D: Appl. Phys.* **2008**, *41*, 115409.
(15) Shao, Q.; Li, H.; Wu, K.; Dong, Y.; Jiang, J. *J. Lumin.* **2009**, *129*, 879.
(16) Yi, L.; Zhou, L.; Wang, Z.; Sun, J.; Gong, F.; Wan, W.; Wang, W. *Curr. Appl. Phys.* **2010**, *10*, 208.
(17) Takai, S.; Sugiura, K.; Esaka, T. *Mater. Res. Bull.* **1999**, *34* (2), 193.
(18) Huang, Y.; Seo, H. J.; Zhu, W. *J. Mater. Sci.* **2007**, *42*, 5421.
(19) Hazen, R. M.; Finger, L. W.; Mariathasan, J. W. E. *J. Phys. Chem. Solids* **1985**, *46*, 253.
(20) Cascales, C.; Merndez Blas, A.; Rico, M.; Volkov, V.; Zaldo, C. *Opt. Mater.* **2005**, *27*, 1672.
(21) Kuz'micheva, G. M.; Lis, D. A.; Subbotin, K. A.; Rybakov, V. B.; Zharikov, E. V. *J. Cryst. Growth* **2005**, *275* (1−2), e1835.
(22) Voron'ko, Y. K.; Subbotin, K. A.; Shukshin, V. E.; Lis, D. A.; Ushakov, S. N.; Popov, A.; Zharikov, E. V. *Opt. Mater.* **2006**, *29*, 246.
(23) Méndez-Blas, A.; Rico, M.; Volkov, V.; Zaldo, C.; Cascales, C. *Phys. Rev. B* **2007**, *75*, 174208.
(24) Volkov, V.; Cascales, C.; Kling, A.; Zaldo, C. *Chem. Mater.* **2005**, *17*, 291.
(25) Cascales, C.; Serrano, M. D.; Esteban-Betegón, F.; Zaldo, C.; Peters, R.; Petermann, K.; Huber, G.; Ackermann, L.; Rytz, D.; Dupre, C.; Rico, M.; Liu, J.; Griebner, U.; Petrov, V. *Phys. Rev. B* **2006**, *74*, 174114.
(26) Hanuza, J.; Benzar, A.; Haznar, A.; Maczka, M.; Pietraszko, A.; van der Maas, J. H. *Vib. Spectrosc.* **1996**, *12*, 25.
(27) Rybakova, T. P.; Trunov, V. K. *Zh. Neorg. Khim.* **1974**, *19*, 1631 (in Russian); *Russ. J. Inorg. Chem. (Transl. Zh. Neorg. Khim.)* **1974**, *19*, 1631 (in English).
(28) Trunov, V. K.; Evdokimov, A. A.; Rybakova, T. P.; Berezina, T. A. *Zh. Neorg. Khim.* **1979**, *24*, 168 (in Russian); *Russ. J. Inorg. Chem. (Transl. Zh. Neorg. Khim.)* **1979**, *24*, 168 (in English).

(29) (a) Pandey, R. K. *J. Phys. Soc. Jpn.* **1974**, *36*, 177. (b) Pandey, R. K. Dilithium Heptamolybdotetragadolinate. U.S. Patent 3,939,252, 1976.

(30) Brixner, L. H. *J. Phys. Soc. Jpn.* **1975**, *38*, 1218.

(31) Lukacevic, E.; Santoro, A.; Roth, R. S. *Solid State Ionics* **1986**, *18−19*, 922.

(32) Zhu, H.; Lin, Y.; Chen, Y.; Gong, X.; Tan, Q.; Luo, Z.; Huang, Y. *J. Appl. Phys.* **2007**, *102*, 063104.

(33) Zhao, W.; Lin, Z.; Zhang, L.; Wang, G. *J. Alloys Compd.* **2011**, *509*, 2815.

(34) Zhao, C.; Yin, X.; Huang, F.; Hang, Y. *J. Solid State Chem.* **2011**, *184*, 3190.

(35) Morozov, V. A.; Mironov, A. V.; Lazoryak, B. I.; Khaikina, E. G.; Basovich, O. M.; Rossell, M. D.; Van Tendeloo, G. *J. Solid State Chem.* **2006**, *179*, 1183.

(36) Arakcheeva, A.; Logvinovich, D.; Chapuis, G.; Morozov, V.; Eliseeva, S. V.; Bünzli, J.-C. G.; Pattison, P. *Chem. Sci.* **2012**, *3*, 384.

(37) (a) Petrícek, V.; Dusek, M.; Palatinus, L. *JANA2000: the crystallographic computing system*; Institute of Physics: Praha, Czech Republic, 2000. (b) Dusek, M.; Petrícek, V.; Wunschel, M.; Dinnebier, R. E.; van Smaalen, S. *J. Appl. Crystallogr.* **2001**, *34*, 398. (c) Brandenburg, K. *DIAMOND*, version 2.1c; Crystal Impact GbR: Bonn, Germany, 1999.

(38) NorECs AS, http://www.norecs.com.

(39) Schaumburg, G. *Dielectric Newsletters*, Mar 1995, Vol. *9*.

(40) Morozov, V. A.; Arakcheeva, A. V.; Chapuis, G.; Guiblin, N.; Rossell, M. D.; Van Tendeloo, G. *Chem. Mater.* **2006**, *18*, 4075.

(41) Arakcheeva, A.; Pattison, P.; Chapuis, G.; Rossell, M.; Filaretov, A.; Morozov, V.; Van Tendeloo, G. *Acta Crystallogr., Sect. B* **2008**, *64*, 160.

(42) De Wolf, P. M.; Janssen, T.; Janner, A. *Acta Crystallogr., Sect. A* **1981**, *37*, 625.

(43) (a) Janssen, T.; Chapuis, G.; de Boissien, M. *Aperiodic Crystals: From Modulated Phases to Quasicrystals; International Union of Crystallography Book Series*; Oxford University Press: Oxford, U.K., 2007. (b) Van Smaalen, S. *Z. Kristallogr.* **2004**, *219*, 681.

(44) (a) Strukov, B.; Shnaidshtein, I.; Onodera, A. *Ferroelectrics* **2008**, *363* (1), 27. (b) Strukov, B.; Onodera, A.; Taraskin, S. A.; Shnaidshtein, I.; Redkin, B. S.; Khara, X. *Zh. Exp. Teor. Phis.* **1995**, *108*, 373 (in Russian); *Russ. J. Exper. and Theor. Phys. (Transl. Zh. Exp. Teor. Phis.)* **1995**, *81* (1), 202.

(45) Ullmann, H.; Trofimenko, N.; Tietz, F.; Stover, D.; Ahmad-Khanlou, A. *Solid State Ionics* **2000**, *138*, 79.

(46) Barsoukov, E., Macdonald, J. R., Eds. *Impedance Spectroscopy, Theory, Experiment and Applications*, 2nd ed.; Wiley-Interscience: New York, 2005.

(47) Boukamp, B. A. *Solid State Ionics* **1986**, *20*, 31.

(48) Samara, G. A. *Solid State Phys.: Adv. Res. Appl.* **1984**, *38*, 1.

(49) Zhang, G. G.; Fang, Q. F.; Wangand, X. P.; Yi, Z. G. *J. Phys.: Condens. Matter* **2003**, *15*, 4135.

(50) Van Herle, J.; McEvoy, A. J.; Thamol, K. R.; Mater, J. *J. Mater. Sci.* **1994**, *29*, 3691.

(51) Inaba, H.; Tagawa, H. *Solid State Ionics* **1996**, *83*, 1.

(52) Kruglyashova, A. L.; Skoub, E. M. *Solid State Ionics* **1988**, *28−30*, 233.

(53) Bottelberghs, P. H.; Broers, G. H. J. *J. Electroanal. Chem. Interfacial Electrochem.* **1976**, *67*, 155.

(54) (a) Liao, J.; Qiu, B.; Lai, H. *J. Lumin.* **2009**, *129*, 668. (b) He, X.-H.; Guan, M.-Y.; Sun, J.-H.; Lian, N.; Shang, T.-M. *J. Mater. Sci.* **2010**, *45*, 118.

(55) Arakcheeva, A.; Chapuis, G. *Acta Crystallogr., Sect. B* **2008**, *64*, 12.

5324

dx.doi.org/10.1021/ic300221m | *Inorg. Chem.* 2012, 51, 5313−5324